Fatigue Crack Growth in a Particulate TiB_2-Reinforced Powder Metallurgy Iron-Based Composite

N. YANG and I. SINCLAIR

Fatigue crack growth behavior has been examined in a particulate titanium diboride (TiB_2)–reinforced iron-based composite that had been produced *via* a mechanical alloying process. Comparison with equivalent unreinforced material indicated that fatigue crack growth resistance in the composite was superior to monolithic matrix material in the near-threshold regime. The composite exhibited relatively low crack closure levels at threshold, indicative of a high intrinsic (effective) threshold growth resistance compared to the unreinforced iron. The lower closure levels of the composite were consistent with reduced fracture surface asperity sizes, attributable to the reinforcement particles limiting the effective slip distance for stage I–type facet formation. The observed shielding behavior was rationalized in terms of recent finite-element analysis of crack closure in relation to the size of crack wake asperities and the crack-tip plastic zone. The different intrinsic fatigue thresholds of the composite and unreinforced iron were closely consistent with the influences of stiffness and yield strength on cyclic crack-tip opening displacements. Cracks in the composite were generally seen to avoid direct crack-tip–particle interaction.

I. INTRODUCTION

PARTICULATE metal matrix composites (PMMCs) have generated significant interest as high specific strength and stiffness materials suitable for a range of aerospace and automotive applications.[1] While specific strength and stiffness are of course critical in many aspects of load bearing structures for the transport industry, components may also be subject to critical size constraints (*e.g.* gears and drive-train parts), where intrinsically high stiffness and strength are necessary. Iron/steels offer the highest Young's modules of common engineering alloys (~210 GPa), with recent work on PMMCs of iron- and steel-based matrices containing particulate titanium diboride (TiB_2) showing that materials may be produced with Young's moduli of up to 285 GPa for a reinforcement content of 30 pct,[2,3,4] while reductions in density are of course also realized by the addition of the reinforcement phase. While failure characteristics are often identified as a limiting factor in the use of structural PMMCs, it has been shown that mechanically alloyed particulate TiB_2/iron–based composites that exhibit clear improvements in strength and stiffness over monolithic material may retain reasonable ductility, notched tensile strength, and fracture toughness levels.[3] As a number of promising potential applications of such composites are in aerospace and automotive components subjected to severe cyclic loads, the fatigue properties are clearly of interest. Fatigue strengths have been reported previously and shown to be superior to equivalent unreinforced materials;[3] however, details of the micromechanisms of failure and the associated implications for crack propagation resistance have not as yet been published.

Previous studies of fatigue crack growth behavior in PMMCs have, to a great extent, concentrated on SiC reinforced aluminum alloys, with various investigators noting the effects of particle morphology and crack-tip–reinforcement interactions on fatigue behavior.[5–12] Shang and Ritchie,[5] for example, have identified marked increases in crack closure levels (and hence crack growth resistance) with increasing SiC_p size between ~5 and 10 μm in a 7091-type aluminum alloy, consistent with a simple increase in scale of crack deflection around larger reinforcement particles. Mason and Ritchie[6] have found that fatigue crack growth thresholds at a load ratio (R) of 0.1 are increased with increasing volume fraction of reinforcement (from 20 to 30 pct) for a SiC_p-reinforced 2124-type aluminum alloy, while threshold levels are essentially constant at $R = 0.7$, which they attribute to reinforcement contributions to crack closure levels. A similar increase in fatigue threshold was also reported with increasing reinforcement content in a SiC_p-reinforced 7091-type aluminum alloy.[5] In terms of crack path deflection due to crack-tip–reinforcement interactions, it has been demonstrated that at lower stress intensity levels, "intact" high stiffness reinforcement particles tend to deflect a propagating crack tip due to local load-transfer processes.[7] This is consistent with crack deflection at reinforcement particles being particularly evident in the near-threshold regime.[8,9,10] Where crack-tip–reinforcement particle interactions do occur at low stress intensity levels, they have been identified with small particle/low reinforcement fraction regions of the composite microstructure in a mechanically alloyed SiC_p-reinforced 2124-type aluminum alloy.[11,12] In a cast SiC_p-reinforced AA356 however, matrix-particle interface failure has been identified with high reinforcement content regions of the material, which may be attributed to weaker interfacial bonding from the casting process.[13] Overall, it may be seen that reinforcement may have distinct influences on "extrinsic" resistance of the crack growth (*i.e.,* crack closure/shielding behavior), while it should be recognized that specific micromechanic processes may be a function of material/processing route combination.

The superior notched strength and fracture toughness of mechanically alloyed particulate TiB_2/iron–based composites has previously been attributed to the uniform distribution of

N. YANG, Engineer, is with Airbus UK, Filton, Bristol, B599 7AN, United Kingdom. I. SINCLAIR, Lecturer, is with the School of Engineering Sciences, Southampton University, Southampton, S017 1BJ, United Kingdom. Contact e-mail: i.sinclair@soton.ac.uk

Manuscript submitted March 12, 2001.

fine TiB_2 obtained through the mechanical milling process.[3] In this article, long fatigue crack growth behavior of a similar iron-based 15 pct vol TiB_2 particle reinforced composite (and corresponding monolithic iron) has been investigated at two load ratios. Crack closure levels were measured to assess the extrinsic and intrinsic crack growth resistance. Quantitative crack path analysis was performed to assess crack-tip–particle interactions as a function of stress intensity level.

II. EXPERIMENTAL

A. *Materials and Microstructures*

The composite selected for this study was pure iron reinforced with 15 pct volume fraction of TiB_2 particles. This composite was processed at DERA (now Qinetiq Ltd., Farnborough, United Kingdom) by a powder metallurgy process, involving a mechanical milling stage before hot-isostatic pressing. Unreinforced pure iron with an equivalent processing history was also obtained as a reference material. Optical micrographs of the composite and unreinforced iron are shown in Figure 1(a) and (b). The TiB_2 particles of the composite are too fine to distinguish in Figure 1(a), although a grain size of ~150 μm is apparent in the etched micrograph. Equiaxed grains of a similar size can also be seen in the unreinforced iron in Figure 1(b).

The room-temperature monotonic mechanical properties of the composite and unreinforced iron are shown in Table I. Increases in the strength and modulus of the composite over the unreinforced iron are apparent, while a reasonable ductility is obtained.

The morphology and distribution (in both size and spatial arrangement) of the TiB_2 particles of the composite were quantified on two-dimensional sections using a finite-body tessellation method,[14] based on scanning electron microscopy (SEM) of the material. A finite-body tessellation consists of a network of cells such that every point within a cell is closer to the interface of the corresponding particle than any other. It has been found previously that such interface-based finite-body tessellation provides a valuable method of assessing particle distributions in common particulate MMC microstructures, offering significant advantages over Dirichlet tessellation and nearest-neighbor methods.[14,15,16] A variety of parameters relating to particle morphology and spatial distribution may then be derived for each individual particle, for instance, "local" area fraction (ratio of particle area and corresponding tessellation cell area), and mean near-neighbor distance (average of the interface-to-interface separations with all particles that share a cell edge around each individual particle of interest). In particular, the coefficient of variation of mean near-neighbor distance ($COV(d_{mean})$), defined as the ratio of the standard deviation and the average of mean near-neighbor distances, has been identified in previous work as a particle-morphology-independent parameter to quantify homogeneity of particle distributions.[15,16] It has been shown that a $COV(d_{mean})$ value of 0.36 ± 0.02 is indicative of a homogeneous (in this context being taken to mean random) particle distribution.[15,16]

Standard image analysis and finite-body tessellation measurements of the present particulate TiB_2 reinforced composite showed that the particles had an average diameter of 0.84 μm (as equivalent area circles) and average aspect ratio of 1.4.

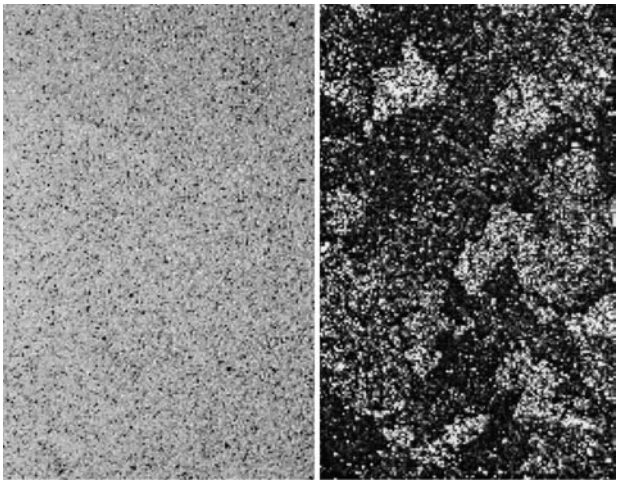

(*a*)

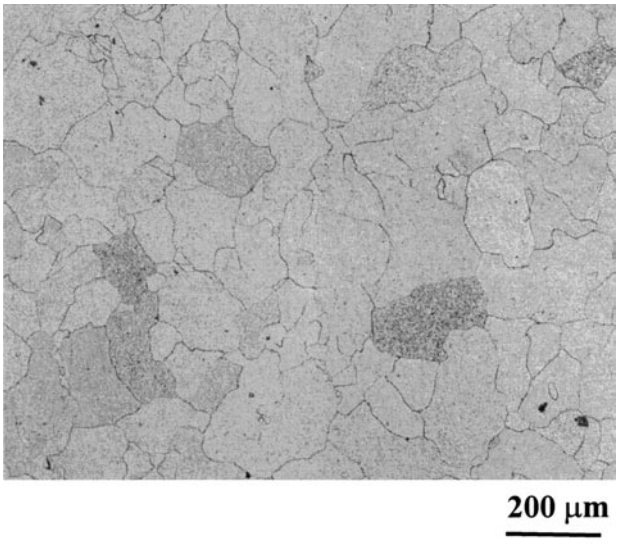

(*b*)

Fig. 1—Optical micrographs of (*a*) particulate TiB_2-reinforced iron-based composite and (*b*) equivalent unreinforced iron.

Table I. Room-Temperature Mechanical Properties of the Composite and Unreinforced Iron

Materials	*E,* GPa	$\sigma_{0.2}$, MPa	El, pct
Fe + 15 Pct − TiB_2	245	260	24.2
Fe	210	135	—

The maximum size of the particles was 4.7 μm for a total of 1100 particles measured. A mean near-neighbor distance of 1.4 μm was obtained, and in particular, a $COV(d_{mean})$ value of 0.40 was recorded, indicative of the reinforcement particles being reasonably well distributed (close to a true random distribution).[15,16] No significant banding or preferential particle orientation was detected.

B. *Fatigue Crack Growth*

Fatigue crack growth tests were carried out using single-edge notched testpieces in four-point bending. Nominal

testpiece dimensions were 60 × 10 × 5 mm. All testpieces were notched to a depth of ~1.5mm using a low speed diamond saw (with a blade thickness of 150 μm), and were then precracked under stress intensity (K) control in accordance with the guidelines of ASTM E 647-95A prior to obtaining fatigue crack growth data. Stress intensities were calculated from solutions provided by Gross and Scrawley.[17] A standard direct-current potential-difference technique was used to measure crack lengths. All tests were performed in laboratory air (18 °C to 22 °C, ~45 pct relative humidity) on an Instron (Canton, MA) 8872 servohydraulic testing machine operating at a sinusoidal loading frequency of 40 Hz. The load ratio (R ratio) was kept constant in each test, with tests being carried out at values of 0.1 and 0.5. In the tests, threshold was first approached (defined here as fatigue crack growth rate (da/dN) $\leq 9 \times 10^{-8}$ mm/cycle) under automated stress intensity control at a normalized K gradient of -0.15 per mm. Once the threshold was reached, the tests were then continued to catastrophic failure at a constant load range that was approximately 5 pct higher than the threshold load range. An exception was for the fatigue tests of the composite at $R = 0.1$, where two testpieces were employed. For one testpiece, testing was initially performed as described previously but was halted once threshold was reached. For the other testpiece, the experiment was performed under constant load range conditions, starting at a stress intensity factor range (ΔK) of ~9 MPa$\sqrt{\text{m}}$ ($da/dN \sim 1 \times 10^{-6}$ mm/cycle),but was halted at a nominal stress intensity range of ~25 MPa$\sqrt{\text{m}}$, *i.e.,* prior to final failure. These two samples were then used for crack path analysis in relation to the surrounding composite microstructure (described further in Section C).

A back-face strain gage was used to obtain compliance data to determine a closure stress intensity, K_{cl}, defined as contact of the crack surfaces on unloading. Compliance measurements were carried out at a frequency of 1 Hz by interrupting the fatigue test periodically, with the compliance data then being averaged over three load cycles. A nonsubjective curve-fitting method was used to measure closure levels (a linear fit was made to the upper linear part of the compliance curve, while a quadratic function was fitted to the lower nonlinear part), the details of which may be found elsewhere.[18]

C. *Crack Profiles and Fractography Analysis*

General aspects of crack growth behavior were assessed *via* crack sections taken parallel to the nominal growth direction. However, for more detailed assessment of crack behavior as a function of stress intensity range, only a limited number of particle-crack tip interaction events can be observed on such "side-on" profiles in tests where K values vary continuously with crack length (as performed here). As such, crack sectioning has also been carried out perpendicular to the crack growth direction in this work. Specifically, the two composite testpieces for which the fatigue tests were suspended prior to failure (*i.e.* for $R = 0.1$ near-threshold and at ΔK ~25 MPa$\sqrt{\text{m}}$) were sectioned and polished near the crack tip to provide a statistically reasonable sample for assessment of particle distribution and associated crack interactions. Using these sections, particle number densities were measured: (a) along the crack path and (b) along randomly spaced test lines in the same overall direction as the crack. Particle cracking and particle-matrix decohesion were carefully identified in enlarged images. A semiquantitative estimate of particle-induced crack deflection was obtained from the line density of particles where "obvious" crack deflection was considered to have occurred. While a rigorous definition of crack deflection and identification of a causal link to any given particle on a two-dimensional section of a three-dimensional body are clearly problematic; it was considered that a first-order indication of the incidence of deflection may be given by counting path deflections (defined as $\geq$30 deg) around individual particles that occurred within a distance of two diameters of the particle interface in question (the diameter being taken from the dimensions of the particle exposed on the sectioning plane). While deflections seen on through-thickness sections of a crack may be identified with maintaining crack front continuity rather than the interactions that occur as a crack-tip advances, the notion that crack path deflections due to the presence of a relatively small particle (in relation to the total crack front length) in the path of a three-dimensional crack should still be reflected in through-thickness sections is considered reasonable.

Side-on crack profiles and fatigue fracture surfaces of the composite and unreinforced iron were also examined along the specimen midthicknesses in the SEM. The side-on profiles were obtained by conventional metallographic sectioning at the specimen midthickness of nickel-plated fracture surfaces. All SEM observations were performed at an accelerating voltage of 15 kV and a specimen tilt angle of 0 deg.

III. RESULTS

A. *Fatigue Crack Growth*

Fatigue crack growth rates of the composite and unreinforced iron are shown in Figures 2 and 3 as a function of nominal (applied) stress intensity range (ΔK_{nom}) for $R = 0.1$ and 0.5, respectively. It may be noted that fatigue crack growth rates for maximum stress intensities (K_{max} values) larger than 20 MPa$\sqrt{\text{m}}$ have been cut-off to maintain small scale yielding conditions given the limited scale of the testpieces. At $R = 0.1$, an applied threshold stress intensity range ($\Delta K_{th.\text{nom}}$) of 7.2 MPa$\sqrt{\text{m}}$ was determined for the composite, and 6.0 MPa$\sqrt{\text{m}}$ for the unreinforced iron. Increasing load ratio to 0.5 decreased $\Delta K_{th.\text{nom}}$ by ~20 pct for the composite and ~10 pct for the unreinforced iron; see to the threshold results summary in Table II. In the Paris regime, *i.e.* between 10^{-6} and 10^{-4} mm/cycle in Figures 3 and 4, the composite exhibited a slightly greater slope than the unreinforced iron at $R = 0.1$, with lower fatigue crack growth resistance in the composite than in the unreinforced iron at ΔK_{nom} levels greater than 11 MPa$\sqrt{\text{m}}$ (Figure 2). At $R = 0.5$, the two materials exhibit very similar Paris-regime slopes, although the composite shows slightly higher fatigue crack growth rates at ΔK_{nom} levels greater than 6 MPa$\sqrt{\text{m}}$ (Figure 3). It is seen from Figures 2 and 3 that the fatigue crack growth resistance of the composite is superior to that of the unreinforced iron in the near-threshold regime both at $R = 0.1$ and 0.5.

A summary of effective stress-intensity ranges at threshold ($\Delta K_{th.\text{eff}}$), along with corresponding crack closure levels ($K_{cl}/K_{\max}$) is shown in Table II for both composite and unreinforced iron at $R = 0.1$ and 0.5, where $\Delta K_{th.\text{eff}} = K_{\max} - K_{cl}$. Values of $K_{cl}/K_{\max}$ were derived *via* curve fitting of backface strain gage data, as noted previously. It has been shown[18] that the curve-fitting method provides a sensitive, low-noise measure of the onset of crack closure. In assessing the curve-fitting method of closure measurement, Xu *et al.*[18,19] note the potential confusion in measuring crack closure levels in conventional plain-sided (non-side-grooved) test specimens, showing that closure measurements made on such specimens may be influenced by "premature" crack face contact occurring at the specimen surfaces (*i.e.,* under plane stress conditions), even though growth rates are demonstrably plane strain controlled. As such, many conventional closure measurements may not genuinely reflect the closure processes that are in fact controlling crack growth. To minimize this effect in the current work, closure results at threshold are only considered, minimizing any complication of mixed stress state effects on growth rate behavior and closure measurements.

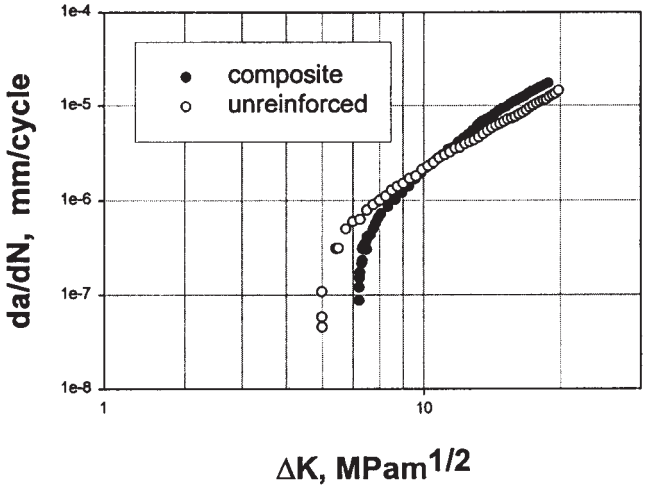

Fig. 2—Fatigue crack growth rates of particulate TiB_2-reinforced iron-based composite and equivalent unreinforced iron at $R = 0.1$.

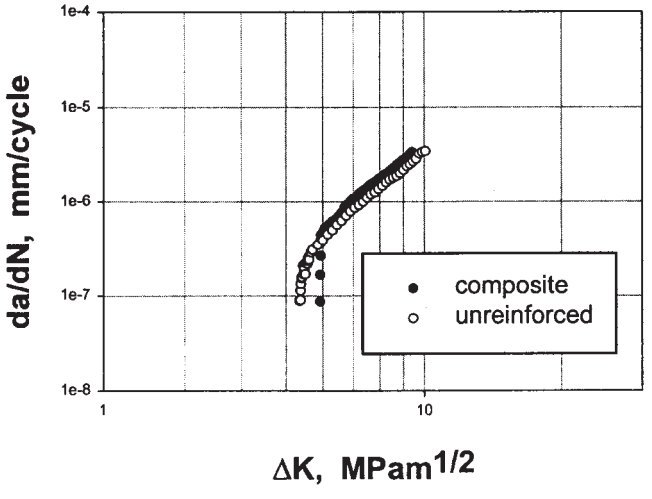

Fig. 3—Fatigue crack growth rates of particulate TiB_2-reinforced iron-based composite and equivalent unreinforced iron at $R = 0.5$.

It may be seen from Table II that crack closure was detected at threshold at $R = 0.1$ and 0.5 for both materials. It may be seen that $\Delta K_{th.\text{eff}}$ values for $R = 0.1$ and 0.5, based on these closure measurements, are quite consistent for each material, inferring a distinct dependency of crack growth on closure. It is also apparent from Table II that the unreinforced iron exhibits significantly higher values of $K_{cl}/K_{\max}$ than the composite at threshold for corresponding load ratios. As such, the improved apparent threshold resistance of the composite (*i.e.,* $\Delta K_{th.\text{nom}}$) is attributable to intrinsic material behavior, although the effect is moderated by reduced closure levels.

B. *Crack Path Analysis*

A typical crack profile and associated surrounding microstructure is shown in Figure 4 (obtained by sectioning perpendicular to the growth direction). Table III shows the number densities of interfacial debonding, particle fracture, and deflection obtained from particle-number counting along crack paths and along randomly placed straight lines. In the first instance, it is seen that the interfacial debonding of particles is much more common than particle fracture, indicating that interfacial strength is the more limiting factor in fatigue damage accumulation in these composites. The total density of debonded and cracked particles is significantly smaller than that obtained from random straight lines, indicating that the cracks specifically avoid direct particle interactions at both threshold (7.3 MPa$\sqrt{\text{m}}$) and higher ΔK_{nom} levels (19.0 MPa$\sqrt{\text{m}}$), although the effect is more pronounced at threshold. This would appear to be consistent with the increased incidence of crack deflection at particles that was measured at the lower ΔK level (Table III).

Table II. Fatigue Data of the Composite and Unreinforced Iron

Materials	Stress Ratio R	$\Delta K_{th\ \text{nom}}$	K_{cl}	$\Delta K_{th\ \text{eff}}$
			MPa$\sqrt{\text{m}}$	
Fe	0.1	6.0	3.2	2.8
Fe	0.5	5.3	2.3	3.0
Fe + 15 pct − TiB_2	0.1	7.2	2.8	4.5
Fe + 15 pct − TiB_2	0.5	5.9	1.3	4.6

C. *Fractography*

Side crack profiles for the composite and unreinforced iron at near-threshold ΔK levels are shown in Figures 5(a) and (b). It may be seen that the unreinforced iron exhibits a highly serrated crack path with individual asperity sizes corresponding to the scale of the underlying grain structure, while the crack path of the composite is relatively planar.

Figures 6(a) through (d) are SEM surface morphologies of the composite and unreinforced iron at near-threshold and intermediate ΔK levels: $\Delta K_{nom} \sim 8$ and $\sim 16\ MPa\sqrt{m}$ for the composite and ~ 6 and $\sim 15\ MPa\sqrt{m}$ for the unreinforced iron. At the near-threshold ΔK_{nom} level, the fracture surface of the unreinforced iron exhibits large facets or steps (Figure 6(c)), in keeping with the serrated crack profile identified from the crack profiles. In contrast, the fracture surface of the composite has a much reduced scale of surface roughness (Figure 6(b)). Nevertheless, small angular steps can still be observed on the fracture surface of the composite at the near-threshold ΔK_{nom} level (Figure 6(a)). The scale of these steps is of the same order as the average particle spacing in this composite (*i.e.* 1 to 2 μm, Section II–B). With increasing ΔK_{nom} levels, the extent of crystallographic fracture surface features is reduced for both composite and unreinforced materials, with this effect occurring at generally lower ΔK levels in the composite. A few large fractured and decohered particles can be seen on the surface of the composite at the intermediate ΔK_{nom} level (Figure 6(b)); however, particles are hardly apparent at the near-threshold ΔK_{nom} level, consistent with the previous crack path analysis.

Final fracture surfaces of the composite are also shown in Figures 7(a) and (b). While the fracture surfaces for static failure of the unreinforced iron showed typical ductile behavior, it is interesting to see extensive cleavage facets on the fracture surface of the composite in Figure 7(a), with a facet size comparable to the apparent grain size of the material, as seen in Figure 1(a). Cleavage initiation was identified with fractured TiB_2 particles (Figure 7(b)).

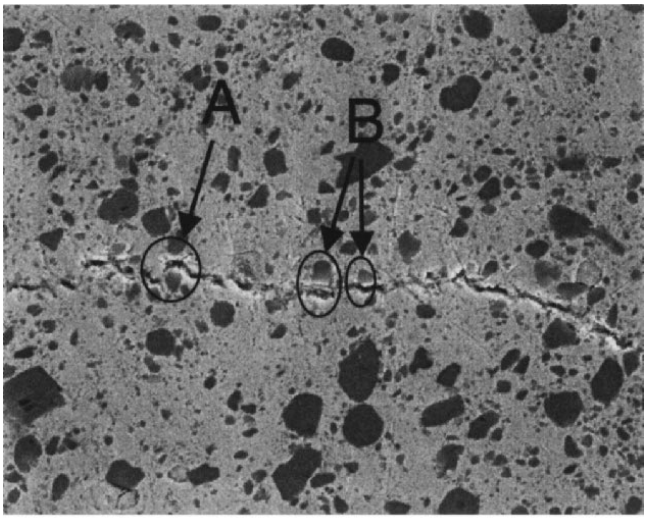

Fig. 4—A typical crack profile (sectioned perpendicular to the fatigue crack growth direction) and associated surrounding microstructure of TiB_2-reinforced iron-based composite at $\Delta K \sim 19\ MPa\sqrt{m}$. Arrows indicate examples of (*a*) crack deflection and (*b*) interfacial debonding.

IV. DISCUSSION

A. *General Aspects of Crack Growth*

It has been shown that fatigue crack growth resistance of the present composite is superior to that of the unreinforced iron in the near-threshold regime. In terms of the failure mechanisms, fractography in Figure 6(a) and path analysis results in Table III indicate that fatigue failure occurs primarily in the matrix at threshold. This is consistent with previous studies in Al-SiC PMMCs, where it has been shown that when fatigue failure is primarily associated with matrix failure, with little contribution from reinforcement fracture or interfacial debonding, particulate/whisker reinforcement may enhance crack growth resistance.[1,6,10,20,21]

In the Paris regime, particle failure or interfacial debonding is expected to be promoted in PMMCs due to increased stress intensities and the associated critical sampling volume ahead of the crack tip. Such reinforcement failure may then of course lead to accelerated crack growth rates, which is commonly manifested by increasing Paris law exponent values.[1] For the materials and test conditions considered here, there was some evidence of accelerated crack growth rates in the composite, although the effect was relatively minor and Paris regime slopes were not particularly high. This is consistent with the fact that the reinforcement particles were not particularly preferred crack paths in the present PMMCs, as indicated by the number density for crack tip–particle interactions being lower than for random lines, even at the higher stress intensity levels sampled here.

It is clear that in the present composites, the incidence and scale over which faceted crack growth occurred at low stress intensities was limited by the presence of reinforcement particles. Given the scale of faceting in the composite and monolithic materials (*i.e.* corresponding to the interparticle spacing and the grain size respectively), there would appear

Table III. Number Density of Particles on Random Test Lines and Number Density of Decohesion, Deflection, or Fracture of Particles on Crack Paths

Stress Intensity Range ΔK,MPa$\sqrt{m}$	Particle Density on Random Test Lines	Interface Decohesion on Crack Paths	Crack Deflection on Crack Paths	Particle Fracture on Crack Paths
	mm^{-1}			
7.3	180	124	37.4	6.5
19.0	180	152	2.8	5.6

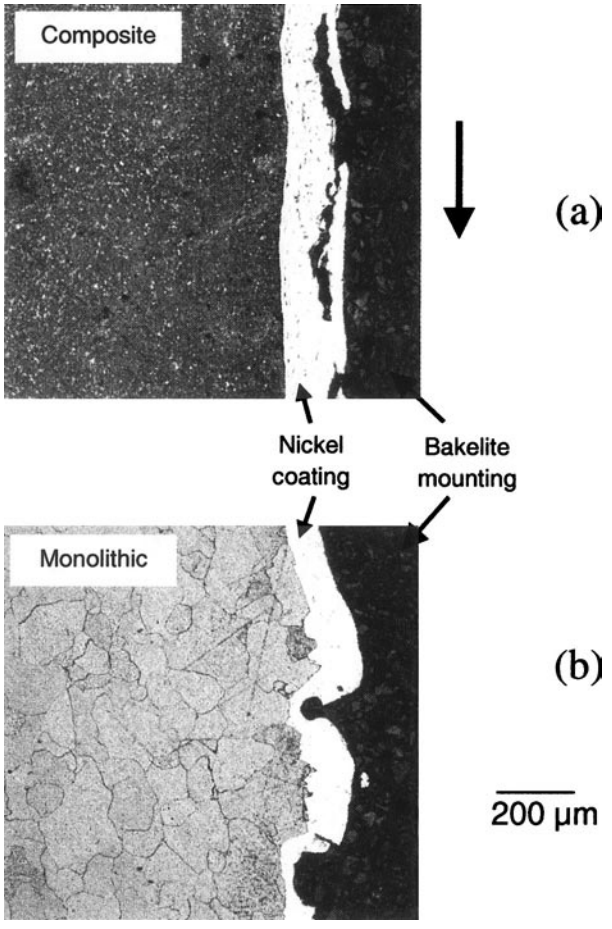

Fig. 5—Side crack profiles (nickel-coated and mounted in bakelite): (*a*) particulate TiB_2-reinforced iron-based composite and (*b*) equivalent unreinforced iron; at the near-threshold stress intensity levels and $R = 0.1$. Vertical arrow indicates general direction of crack growth.

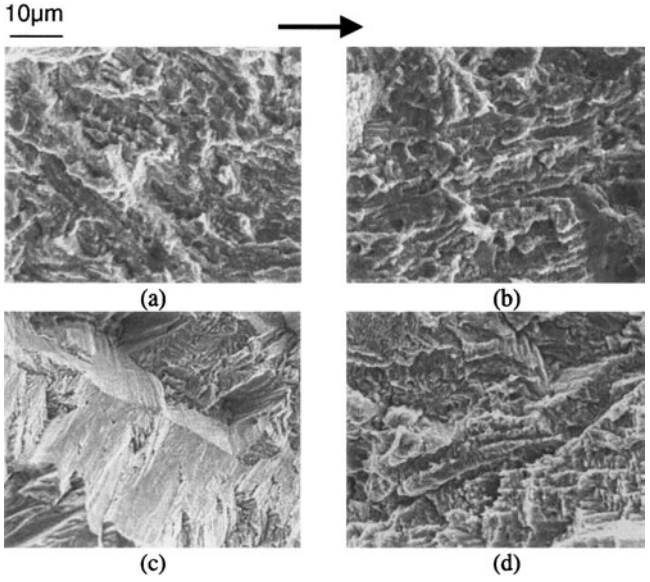

Fig. 6—Fatigue fracture surfaces of (*a*) composite at $\Delta K \approx 8\ \text{MPa}\sqrt{\text{m}}$, (*b*) composite at $\Delta K \approx 16\ \text{MPa}\sqrt{\text{m}}$, (*c*) equivalent unreinforced iron, $\Delta K \approx 6\ \text{MPa}\sqrt{\text{m}}$, and (*d*) equivalent unreinforced iron, $\Delta K \approx 15\ \text{MPa}\sqrt{\text{m}}$. Horizontal arrow indicates general direction of crack growth

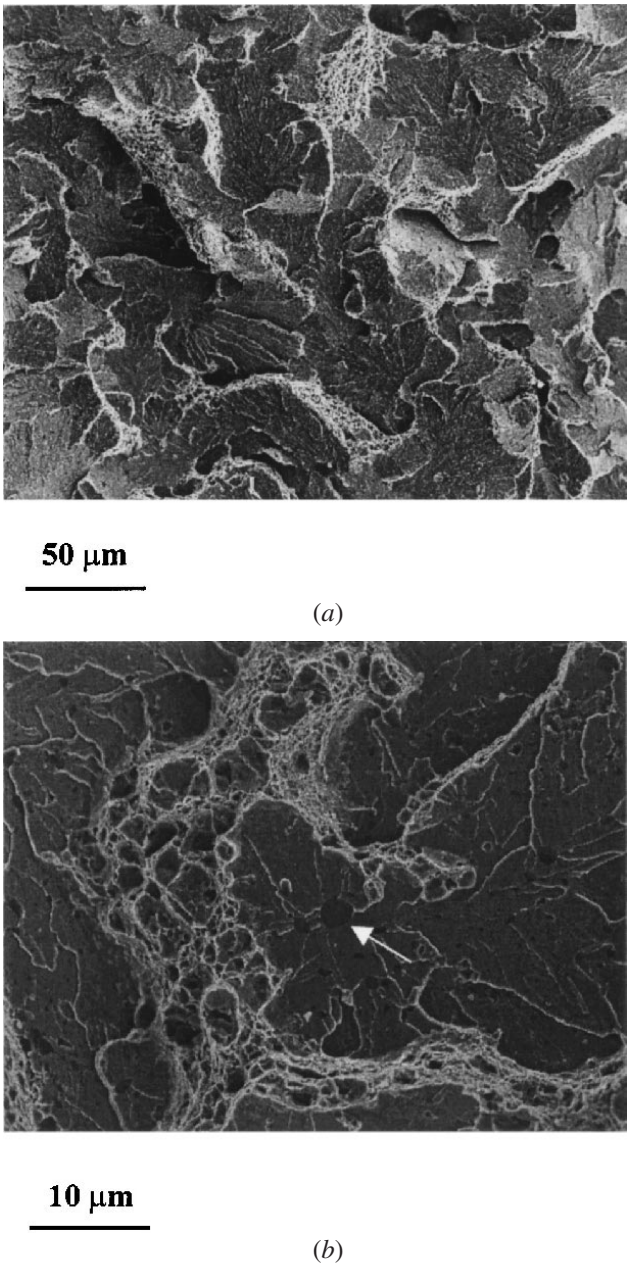

Fig. 7—(*a*) and (*b*) Cleavagelike brittle static failure of particulate TiB_2-reinforced iron-based composite. The arrow in the lower picture indicates a fractured TiB_2 particle from which the cleavage initiated.

to be a simple link between the separation of primary slip blocking features and the extent of crystallographic crack growth in each microstructure. It may be noted that while the threshold monotonic and cyclic plastic zone sizes in the composite were somewhat larger than the mean near-neighbor separation in the composite (Section IV–C), the slip homogenizing effect of the particles did not suppress stage I–type crack growth within the matrix, although there was evidence of stage I suppression at higher ΔK levels.

B. *Crack Closure at Threshold*

Fatigue crack growth rates in the near-threshold regime at low load ratios are commonly thought to be influenced

by crack closure.[22] Roughness-induced crack closure (RICC) is considered to be most significant at threshold at low R ratios, as crack opening displacements may become significantly smaller than fracture surface asperity sizes. Relationships between exact surface geometry and crack closure levels are poorly understood, however it is clear that surface geometry, crack-tip deformation, and surface contact mechanics all contribute to the shielding process. While various articles in the literature identify surface asperity size as a determining factor in measured crack closure levels,[23,24] a first-order dependence of closure level on crack deflection angles (as opposed to size) has been identified theoretically[25] and experimentally.[10] Although various models exist to rationalize different aspects of RICC, Parry *et al.*[26,27] provide the only explicit treatment of both crack path and plasticity effects on closure levels, including the separation of surface asperity size and angle effects. Using established finite-element methods, the influence of surface asperity size on crack closure levels has been studied in two dimensions as a function of stress-intensity levels, with the results identifying a controlling influence of the *relative* sizes of the fracture surface asperities and the maximum plastic zone size (for a given load ratio). Modeling results are shown in Figure 8 for a regular crack deflection angle of 45 deg, in terms of maximum, minimum, and mean closure levels (arising from the progress of the crack tip between individual asperities), as a function of L/r_p, where L is the crack deflection length giving rise to surface asperities and r_p is the plastic zone size. It can be seen that closure levels fall off rapidly for small relative asperity sizes, with a plateau occurring for L/r_p values greater than approximately one. Parry *et al.*[26,27] further show a strong influence of crack deflection angle in the plateau region. In the present experimental work, maximum plastic zone dimensions at threshold are ~366 μm for the unreinforced iron and ~143 μm for the composite (according to Shih's results for plain strain conditions[28]). With crack deflection lengths of the order of the grain size (~150 μm) in the unreinforced iron, and the mean near-neighbor distance (~1.4 μm) in the composite, corresponding L/r_p values are then ~0.5 and 0.01, respectively. While exact correlation of the present experimental results with modeling results such as those in Figure 8 would require rather more detailed treatment of the irregular, three-dimensional nature of the real fracture surfaces, it may be seen that the functionality of Figure 8 and the range of L/r_p values that influence closure are consistent with the low closure levels of the composite.

C. *Intrinsic Fatigue Thresholds*

After accounting for the effects of crack closure on the apparent threshold stress-intensity range, it is seen that the iron-based composite possesses a significantly higher intrinsic threshold than the unreinforced iron, as shown in Table II. In terms of critical cyclic crack-tip opening displacements, such behavior may be attributed to increased modulus and flow stress in the reinforced material (Table I). Values of the plane strain effective cyclic crack-tip opening displacement at threshold $\Delta\delta_{th.\mathrm{eff}}$ for the composite and unreinforced iron may be calculated from[28]

$$\Delta\delta_{th.\mathrm{eff}} = 0.49\frac{\Delta K^2_{th.\mathrm{eff}}}{2\,E\sigma_y} \qquad [1]$$

Equation [1] is not necessarily applicable to a multiphase system, although two limiting cases may be identified with the yield stress value that is used: (1) the bulk composite yield strength, where the extent of plasticity is sufficient to sample the overall composite properties; and (2) the matrix yield strength, where plasticity is small in relation to the interparticle separation distance and effectively occurs in the matrix only. The latter case should be seen as a significant simplification, as load transfer may then also be considered to reduce the effective stress intensity in the matrix in this case, and local residual stress effects may also become significant.[29] In terms of the present work, it may be noted that the monotonic and cyclic plastic zone sizes in the composite at threshold were of the order of 160 and 100 times the mean near-neighbor separation distance, and, as such, the bulk composite flow stress is considered reasonable to describe crack-tip deformation. Using the composite bulk flow properties and assuming a critical $\Delta\delta_{th.\mathrm{eff}}$ value at threshold, Eq. [1] predicts an increase in the effective threshold stress intensity range of ~50 pct for the composite material over the unreinforced iron, which compares well with the experimental difference between the unreinforced iron of 57 pct.

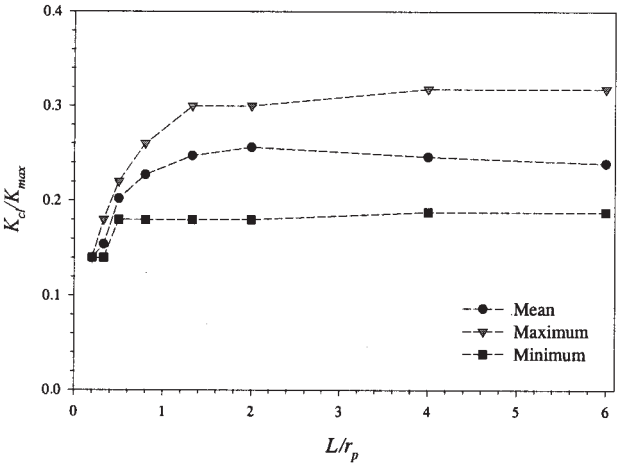

Fig. 8—Finite-element simulation results from Ref. 27, showing effects of varying relative asperity size (L/r_p) on crack closure level ($K_{cl}/K_{\max}$) at a crack deflection angle of 45 deg.

V. CONCLUSIONS

1. The introduction of TiB_2 particles into pure iron through a mechanical milling route results in an increase in apparent threshold stress intensity factor ranges from 6.0 to 7.2 MPa$\sqrt{\mathrm{m}}$ at $R = 0.1$ and from 5.3 to 5.9 MPa$\sqrt{\mathrm{m}}$ at $R = 0.5$.
2. The particulate TiB_2 reinforced iron-based composite develops a relatively planar fatigue fracture surface in the near-threshold regime, consistent with its lower crack closure levels at threshold. Conversely, the unreinforced iron exhibits relatively rough surfaces and hence high closure levels.

Closure measurements rationalized the load ratio effect on threshold in both composite and unreinforced iron. Observed closure behavior and fracture surface morphologies were seen to be consistent with previous elastic-plastic FE simulation of roughness-induced crack closure processes.

3. The particulate TiB_2 reinforced iron-based composite has a higher intrinsic stress-intensity range ($\Delta K_{th.\text{eff}}$) than the unreinforced iron. The intrinsic threshold behavior of the composite and unreinforced iron may be explained through closure-corrected cyclic crack-tip opening displacements.
4. In this composite, cracks tended to avoid direct particle interaction at the stress-intensity conditions considered; this is more obvious in the near-threshold regime. Particle-matrix debonding was found to be the primary particle failure mode in fatigue.

ACKNOWLEDGMENTS

The authors are grateful to Drs. Andrew Wisbey and Zefira Kulikowski, DERA (Farnborough, UK), for provision of the materials, useful discussion, and permission to publish this work.

REFERENCES

1. I. Sinclair and P.J. Gregson: *Mater. Sci. Technol.,* 1997, vol. 13, pp. 709-26.
2. P.S. Goodwin, T.M.T. Hinder, A. Wisbey, and C.M. Ward-Close: *Mater. Sci. Forum,* 1998, vols. 269–272, pp. 53-62.
3. Z. Kulikowski, A. Wisbey, T.M.T. Godfrey, P.S. Goodwin, and H.M. Flower: *Mater. Sci. Technol.,* 2000, vol. 16, pp. 925-28.
4. K. Tanaka, T. Oshima, and T. Saito: *THERMEC*'97, Int. Conf. on Thermomechanical Processing of Steels & Other Materials, T. Chandra and T. Sakai, eds., Tms, Warrendale, PA, 1997, pp. 1279-85.
5. J.K. Shang and R.O. Ritchie: *Acta Metall.,* 1989, vol. 37, pp. 2267-78.
6. J.J. Mason and R.O. Ritchie: *Mater. Sci. Eng.,* 1997, vol. A231, pp. 170-82.
7. A.J. Padkin, M.F. Brereton, and W.J. Plumbridge: *Mater. Sci. Technol.,* 1987, vol. 3, pp. 217-23.
8. J.K. Shang, W. Yu, and R.O. Ritchie: *Mater. Sci. Eng.,* 1988, vol. A102, pp. 181-92.
9. S. Kumai, J.E. King, and J.F. Knott: *Fat. Fract. Eng. Mater. Struct.,* 1992, vol. 15, pp. 1-11.
10. J. Llorca, J. Ruiz, J.C. Healy, M. Elices, and C.J. Beevers: *Mater. Sci. Eng.,* 1994, vol. A185, pp. 1-15.
11. J. Boselli, P.D. Pitcher, P.J. Gregson, and I. Sinclair: *Scripta Mater.,* 1998, vol. 38, pp. 839-44.
12. J. Boselli: Ph.D. Thesis, University of Southampton, Southampton, United Kingdom, 1999.
13. Z. Wang and R.J. Zhang: *Acta Metall.,* 1994, vol. 42, pp. 1433-45.
14. J. Boselli, P.D. Pitcher, P.J. Gregson, and I. Sinclair: *J. Microsc.,* 1999, vol. 195, pp. 104-12.
15. N. Yang, J. Boselli, P.G. Gregson, and I. Sinclair: *Mater. Sci. Technol.,* 2000, vol. 16, pp. 797-805.
16. N. Yang, J. Boselli, and I. Sinclair: *J. Microsc.,* 2001, vol. 201, pp. 189-200.
17. B. Gross and J.E. Srawley: *J. Test Eval.,* 1983, vol. 11, pp. 357-59.
18. Y. Xu, P.J. Gregson, and I. Sinclair: *Mater. Sci. Eng.,* 2000, vol. A284, pp. 114-25.
19. Y. Xu: Ph.D. Thesis, University of Southampton, Southampton, United Kingdom, 2001.
20. T. Christman and R. Suresh: *Mater. Sci. Eng.,* 1988, vol. 102, pp. 211-16.
21. M. Levin and B. Karlsson: *Mater. Sci. Technol.,* 1991, vol. 7, pp. 596-607.
22. R.O. Ritchie: *Mater. Sci. Eng.,* 1988, vol. A103, pp. 15-28.
23. K.T. Venkateswara Rao and R.O. Ritchie: *Int. Met. Rev.,* 1992, vol. 37, pp. 153-85.
24. K.T. Venkateswara Rao, W. Yu, and R.O. Ritchie: *Metall. Trans. A,* 1988, vol. 19A, pp. 549-60.
25. S. Suresh and R.O. Ritchie: *Metall. Trans. A,* 1982, vol. 13A, pp. 1627-31.
26. M.R. Parry, S. Syngellakis, and I. Sinclair: *Mater. Sci. Eng.,* 2000, vol. A291, pp. 224-34.
27. M.R. Parry: Ph.D. Thesis, University of Southampton, Southampton, United Kingdom, 2001.
28. C.F. Shih: *J. Mech. Phys. Solids,* 1981, vol. 29, pp. 305-26.
29. J. Boselli, P.D. Pitcher, P.J. Gregson, and I. Sinclair: *Mater. Sci. Eng.,* 2001, vol. 300, pp. 115-26.